ARTICLE

Check for updates

Current-controlled nanomagnetic writing for reconfigurable magnonic crystals

Jack C. Gartside [1,4✉], Son G. Jung [1,3,4], Seung Y. Yoo [1,4], Daan M. Arroo [2], Alex Vanstone[1], Troy Dion[1,3], Kilian D. Stenning [1] & Will R. Branford [1]

Strongly-interacting nanomagnetic arrays are crucial across an ever-growing suite of technologies. Spanning neuromorphic computing, control over superconducting vortices and reconfigurable magnonics, the utility and appeal of these arrays lies in their vast range of distinct, stable magnetization states. Different states exhibit different functional behaviours, making precise, reconfigurable state control an essential cornerstone of such systems. However, few existing methodologies may reverse an arbitrary array element, and even fewer may do so under electrical control, vital for device integration. We demonstrate selective, reconfigurable magnetic reversal of ferromagnetic nanoislands via current-driven motion of a transverse domain wall in an adjacent nanowire. The reversal technique operates under all-electrical control with no reliance on external magnetic fields, rendering it highly suitable for device integration across a host of magnonic, spintronic and neuromorphic logic architectures. Here, the reversal technique is leveraged to realize two fully solid-state reconfigurable magnonic crystals, offering magnonic gating, filtering, transistor-like switching and peak-shifting without reliance on global magnetic fields.

---

[1] Blackett Laboratory, Imperial College London, London SW7 2AZ, UK. [2] London Centre for Nanotechnology, University College London, London WC1H 0AH, UK. [3] Cavendish Laboratory, University of Cambridge, Cambridge CB3 0HE, UK. [4]These authors contributed equally: Jack C. Gartside, Son G. Jung, Seung Y. Yoo. ✉email: j.carter-gartside13@imperial.ac.uk

Versatile, low-power means to selectively control magnetization states at the nanoscale are critical across a host of applications, both in fundamental science and device-oriented systems. Alongside mature technologies such as data storage, nanomagnetic arrays support a host of more recent applications including neuromorphic computation[1–5], superconducting vortex control[6–9] and reconfigurable magnonic crystals[10–14] (RMCs). RMCs are nanopatterned metamaterials harnessing varying magnetic configurations to manipulate and store information by tuning magnonic (spin-wave) dynamics[15–26].

RMCs promise to be key functional elements in the burgeoning field of magnonics[13,16–19,21,22]. Comprising arrays of interacting nanomagnets, different magnetization configurations of the array (or 'microstates') allow a range of functional behaviours including amplifying and attenuating specific frequency channels[27–31] or bandgap creation and tuning[32–34]. Existing magnonic crystal designs have shown strong initial promise, but are severely limited by a lack of practical means to access more than a handful of microstates. N-element arrays possess 2^N microstates and, typically, systems with 2^{10}–2^{100} potential microstates are restricted to operating within just two or three configurations[11], imposing a hard limit on scope and utility.

Of the existing microstate control techniques, from simple applications of system-wide magnetic fields to Oersted-field stripline techniques and intricate multilayered spin-transfer torque devices[35–38], few are able to selectively reverse the magnetization of an arbitrary element in a strongly interacting nanoarray without affecting neighbouring elements. Many approaches struggle to function without disturbing delicate magnetic states elsewhere in the system due to large stray fields or a reliance on global external fields. The remaining methods rely on mechanical apparatus orders of magnitude larger than the nanomagnet, either a hard-disk style write-head or scanning-probe with magnetic tip[39–41]—unsuitable for on-chip integration and susceptible to damage.

To address the pressing need for non-invasive, global-field free means for nanomagnetic writing, we build on the fundamental principles of 'topological magnetic writing'[39] to present a scheme enabling low-power, fully solid-state access to the entire microstate space of strongly interacting nanomagnetic systems. The tightly localized stray field of a current-driven 180° transverse domain wall (DW) in a nanowire is used to induce dynamic topological defects in adjacent ferromagnetic (FM) nanoislands, driving magnetic reversal. Topological defects in planar nanomagnets are conserved quasi-particles protected by energies on the order of the exchange interaction, granting the writing method strong thermal stability and tolerance for patterning imperfections[42–44]. By varying the drive-current amplitude in the nanowire, fully selective reversal is achieved and nanoislands may be switched or 'skipped' at will as the DW passes. The versatility and utility of the technique are demonstrated via two active magnonic system designs: a reconfigurably gateable one-dimensional (1D) transmission-line RMC optimized for travelling-wave magnons supporting multiple gate types and on/off ratios up to 35 and a two-dimensional (2D) RMC optimized for standing-wave magnons with single-frequency on/off ratios of up to 9×10^3 and mode shifting of $\Delta f = 0.96$ GHz.

Results and discussion
Working principle of reversal method.
The reversal process is depicted schematically in Fig. 1a–d with a corresponding time evolution series shown in Fig. 1e. The system comprises a FM DW-carrying 'control' nanowire (here Permalloy (Py)) and Ising-like Py 'bit' nanoisland(s) at a height h below the control wire.

The control wire serves as a track allowing a transverse control-DW (hereafter c-DW) to traverse the nanoislands via current-induced spin-transfer torque. The c-DW stray field influences the nanoisland magnetizations as it moves over them, allowing the islands to serve as rewritable bits. N.B. the c-DW nomenclature serves just to distinguish the control-nanowire DW from DWs in the bit nanoislands. All DWs discussed are standard transverse DWs. Figure 1e shows a detailed micromagnetic time evolution of the reversal process. Here we view a single Py nanoisland from above (positive z-direction, nanoisland in the xy-plane) as traversed by a c-DW (white circle) in the Py control nanowire, moving with $v_{c-DW} = +\hat{x}$. The nanoisland is initially magnetized with $M = -\hat{y}$ and the chirality of the c-DW such that its magnetization at the c-DW centre points in the $-\hat{z}$ direction towards the nanoisland. The nanoisland dimensions are $400 \times 75 \times 5$ nm³ and the nanowire has quasi-infinite length, 40×40 nm² cross-section and suspension height $h = 10$ nm above the nanoisland.

As the c-DW approaches the nanoisland (Fig. 1e, $t = 0.6$ ns), the c-DW stray-field $\mathbf{H}_{DW}$ distorts the spins on the left edge of the nanoisland, forcing them out of a collinear state to lie along the locally divergent radial $\mathbf{H}_{DW}$. This distortion of the nanoisland magnetization introduces a pair of edge-bound topological defects with opposite polarity ±1/2 winding numbers[43], seen on the nanoisland left edge. Winding numbers in a ferromagnet are conserved and must sum to 1 in a hole-free nanoisland. As the c-DW progresses across the nanoisland ($t = 0.65$ ns), the influence of $\mathbf{H}_{DW}$ extends to the nanoisland's right edge, eventually causing a corresponding pair of edge-bound ∓1/2 topological defects to form ($t = 0.7$ ns).

Continuous chains of reversed spins now connect each topological defect pair across the nanoisland width, effectively binding the ±1/2 defects together via the exchange-energy penalty for breaking the spin chains. Each bound defect pair constitutes a 180° DW; however, the two nanoisland DWs (hereafter i-DWs) are formed asymmetrically. The lower (y-direction) i-DW directly under the c-DW path (dashed white arrow in panel $t = 0.6$ ns) forms in its lowest-energy straight conformation parallel to the nanoisland width, as $\mathbf{H}_{DW}$ is locally oriented along this axis. For the upper i-DW, $\mathbf{H}_{DW}$ is oriented in the positive y-direction antiparallel to the initial nanoisland magnetization. This forces the nascent upper i-DW to assume a contorted conformation around the growing $M = +\hat{y}$ domain (yellow–green region in Fig. 1e), with a corresponding exchange-energy penalty relative to the straight lower i-DW. The difference in nascent i-DW conformations is seen in $t = 0.65$ ns, with the lower, straight and upper, contorted i-DWs highlighted by long and short grey dashed lines, respectively.

Once the c-DW progresses far enough to introduce topological edge defects to the nanoisland's far side, the $M = +\hat{y}$ domain is fully formed and the contorted i-DW no longer forced to assume a high-energy conformation. As such it rapidly straightens out, assuming a low-energy conformation straight across the nanoisland width and converting its excess exchange energy into motion in the process. The released exchange energy propels the i-DW along the nanoisland in the positive y-direction until it collides with the nanoisland's upper end. Upon reaching the island end the ±1/2 defects are free to reach and annihilate each other, unwinding the i-DW to a collinear state and emitting a spin-wave burst down the nanoisland ($t = 0.9$ ns). The spin-wave burst interacts with the remaining i-DW[39,41,45], exerting a torque that accelerates it towards the nanoisland bottom ($t = 1.3$ ns). As the remaining i-DW approaches the nanoisland bottom, it is increasingly magnetostatically attracted to it, further driving acceleration ($t = 2.0$ ns) until the i-DW unwinds on contact as
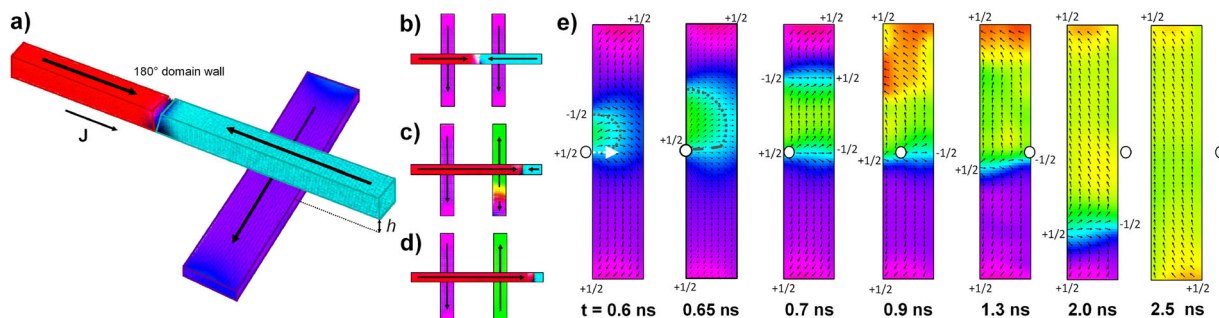
Fig. 1 Schematic of the magnetic reversal method. a Representation of the ferromagnetic domain wall-carrying 'control' nanowire and 'bit' nanoisland, separated by a non-magnetic gap of height h. **b–d** Time-evolution series of the magnetic reversal process in two-nanoisland system. Both nanoislands are initially magnetized with $M = -\hat{y}$ (**b**) before the current-driven 'control' domain wall (c-DW) traverses the right-hand nanoisland, inducing magnetization reversal (**c**), leaving it magnetized $M = +\hat{y}$, whereas the left-hand nanoisland remains unswitched (**d**). It is noteworthy that the internal domain wall structure in **c** and **d** is slightly distorted by the drive-current; **b** shows the static, relaxed domain wall state. **e** Detailed time-evolution series of the reversal process in a single $400 \times 75 \times 5\,nm^3$ nanoisland. The dynamic c-DW is represented by the white circle traversing the nanoisland midpoint, moving with $v_{c-DW} = +\hat{x}$. $t = 0\,s$ is defined when the c-DW begins moving from its origin, 112 nm to the nanoisland's left. The partially formed contorted nanoisland domain wall is highlighted in $t = 0.6\,ns$ by the dashed grey line, with the partially formed straight island domain wall highlighted by longer grey dashes in $t = 0.65\,ns$. Topological defects are labelled with their winding numbers. Corresponding time-evolution series are provided in Supplementary Movies 1–6.

described above, leaving a DW-free nanoisland magnetized antiparallel to its initial state ($t = 2.5\,ns$) with reversal completed ~2 ns after the c-DW reaches the nanoisland.

Distinct modes of reversal method. The process above describes the core physics behind the reversal process, however the Oersted-field $\mathbf{H}_{Oe}$ arising from the drive-current through the control nanowire has not yet been considered. In the absence of $\mathbf{H}_{Oe}$ (for instance, if the c-DW was driven via global $\mathbf{B}$ field), the reversal process occurs as described previously for all permutations of Ising-like initial nanoisland magnetizations ($M = \pm\hat{y}$) and c-DW trajectories ($v_{c-DW} = \pm\hat{x}$). However, reversing the c-DW velocity when driving via current requires reversing the current direction and therefore the direction of $\mathbf{H}_{Oe}$ in the nanoisland plane ($\pm y$-direction). This leads to two distinct reversal regimes occurring at different nanowire suspension heights: a fully selective mode where $h = 20–5\,nm$, allowing reversal of any desired element in a nanoarray, and a close-proximity mode allowing nanoisland reversal at lower current density and higher bit-density than $\mathbf{H}_{Oe}$ stripline-based techniques occurs where $h = 2–11\,nm$, albeit at reduced selectivity relative to the $h = 20–25\,nm$ mode. Nanoislands of dimensions $400 \times 75 \times 5\,nm^3$ are considered in both reversal regimes.

Close-proximity, low-power reversal mode. Considering first the close-proximity mode, here the contorted high-energy i-DW is injected with sufficient energy to overcome the influence of both possible $\pm\hat{y}\mathbf{H}_{Oe}$ directions and will unwind into its nearest nanoisland end as the c-DW passes as in Fig. 1e, $t = 0.7–0.9\,ns$. However, the behaviour of the initially static low-energy i-DW is determined by the drive-current polarity and corresponding $\mathbf{H}_{Oe}$ direction. Figure 2 shows the low-energy i-DW driven 'favourably' (a) by an $\mathbf{H}_{Oe}$ aligned antiparallel to the initial nanoisland magnetization—unwinding at the opposite nanoisland end as the high-energy i-DW and successfully mediating reversal, or 'unfavourably' (b) by an $\mathbf{H}_{Oe}$ parallel with the initial island magnetization—unwinding at the same end as the high-energy i-DW, leaving an unswitched nanoisland magnetized along its initial direction. The dependence of reversal success on initial nanoisland magnetization is illustrated in Fig. 2c, where a four-nanoisland array is prepared in a mix of 'favourable' (islands 1 and 4) and 'unfavourable' initial magnetization states. After

c-DW traversal, only the favourably magnetized islands are reversed.

Successful reversal therefore requires an $\mathbf{H}_{Oe}$ aligned antiparallel to the initial nanoisland magnetization. This means that in the close-proximity regime microstates may be written from a collinear initial state (all nanoislands identically magnetized) such that every nanoisland traversed by the c-DW is switched, with the halting point of the c-DW decided by the user. For instance, in a field-saturated ten-island array with c-DW initialized left of the array, island 1 could be switched, or islands 1–5, but island 5 could not be switched without reversing islands 1–4. For the $400 \times 75 \times 5\,nm^3$ nanoislands considered here the close-proximity mode functions with a minimum current density of $\mathbf{J} = 3 \times 10^{12}\,A/m^2$ for 5 nm-thick Py nanoislands, a factor of 2.3× lower than the minimum $\mathbf{J}$ required for conventional non-selective $\mathbf{H}_{Oe}$ reversal of matching nanoisland and nanowire dimensions. As power consumption and Joule heating scale as $\mathbf{J}^2$, c-DW-driven reversal leads to an 82% reduction in power consumption compared to using only the Oersted field while still affording partial selectivity.

The upper bound of $h = 11\,nm$ is given for close-proximity reversal as for lower separations, the minimum $\mathbf{J}$ required to overcome magnetostatic attraction between c-DW and nanoisland and move the c-DW across the island will also generate sufficient $\mathbf{H}_{Oe}$ to switch the nanoisland, negating 'skip' events where the c-DW passes a nanoisland without switching it and hence preventing full selectivity. Increments of 0.5 nm were considered for h down to a minimum of $h = 2\,nm$.

Fully selective reversal mode. In the fully selective $h = 20–25\,nm$ regime, the increased nanowire–nanoisland separation means the magnitude of the c-DW stray field $\mathbf{H}_{DW}$ at the nanoisland is lower than the critical nucleation field $\mathbf{H}_N$ required to overcome exchange energy and begin locally rearranging spins to nucleate a nascent domain; hence, $\mathbf{H}_{DW}$ alone is unable to drive reversal. However, when combined with a sufficient magnitude $\mathbf{H}_{Oe}$ such that $\mathbf{H}_{DW} + \mathbf{H}_{Oe} \geq \mathbf{H}_N$, reversal occurs as described above. This allows for two current-driving operations to be performed as shown in Fig. 2d: a 'skip' event ($t = 1.7\,ns$), where a low current-density pulse $\mathbf{J} = 1.5–3.0 \times 10^{12}\,A/m^2$ is used to move the c-DW over a nanoisland, while maintaining an $\mathbf{H}_{Oe}$ magnitude below the reversal threshold, and a 'write' event ($t = 2.9\,ns$) where a higher current-density pulse $\mathbf{J} = 5.0–7.0 \times 10^{12}\,A/m^2$ is used to
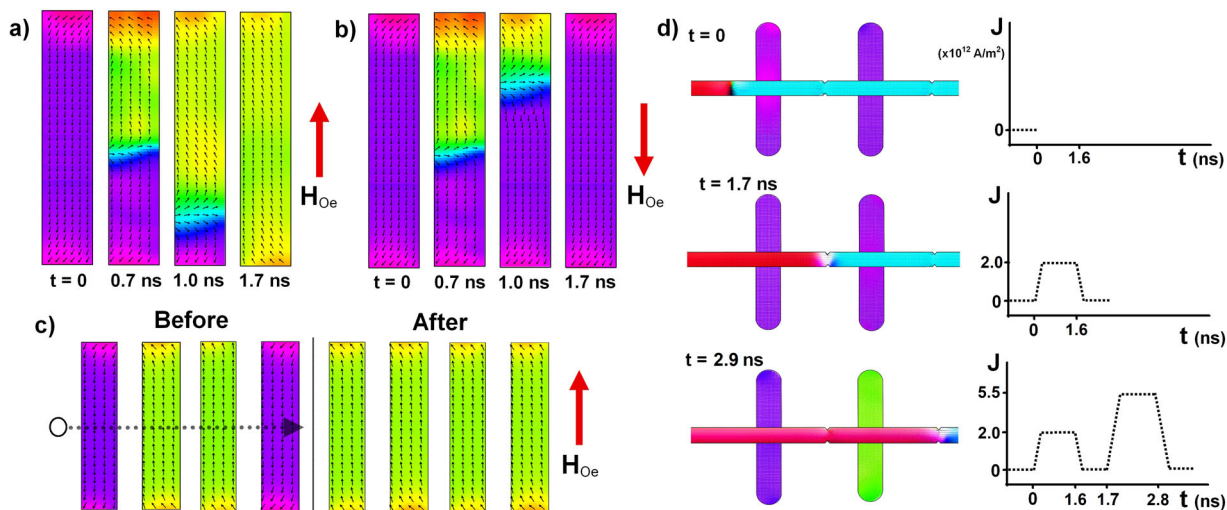
Fig. 2 Close-proximity and fully selective reversal modes. a–c Close-proximity reversal mode. **d** Fully selective reversal. **a** With Oersted-field $\mathbf{H}_{Oe}$ antiparallel to the initial nanoisland magnetization $\mathbf{H}_{Oe}$ aids reversal, driving the low- and high-energy nanoisland domain walls (i-DWs) to opposite nanoisland ends and achieving successful switching. **b** With $\mathbf{H}_{Oe}$ aligned to the initial nanoisland magnetization, the reversal process is hindered, $\mathbf{H}_{Oe}$ drives the low- and high-energy i-DWs into the same nanoisland end, resulting in failed switching. **c** Four-island array initialized ('before' panel) with second and third islands in $M = +\hat{y}$ state, and first and fourth in $M = -\hat{y}$ state. Control domain wall (c-DW) is then driven across the array such that $\mathbf{H}_{Oe} = +\hat{y}$, driving successful reversal of $M = -\hat{y}$ islands (as described in **a**) and failed reversal of $M = +\hat{y}$ islands (as in **b**). **d** c-DW begins to the left of two nanoislands ($t = 0$). It is driven over the first nanoisland by a $\mathbf{J} = 2.0 \times 10^{12}$ A/m^2 'skip' current pulse, leaving the nanoisland unswitched as $\mathbf{H}_{Oe} + \mathbf{H}_{DW} <$ $\mathbf{H}_N$, the nucleation field. The c-DW is then driven over the second nanoisland with a $\mathbf{J} = 5.5 \times 10^{12}$ A/m^2 'write' pulse, switching the nanoisland magnetization as $\mathbf{H}_{Oe} + \mathbf{H}_{DW} \geq \mathbf{H}_N$.

move the c-DW, while providing a sufficiently high $\mathbf{H}_{Oe}$ such that magnetic reversal occurs (Fig. 2d), $t = 1.4$ ns). By combining sequences of these 'skip' and 'write' events, any desired microstate may be realized. To allow for reliable position-control of the c-DW, 5 nm notches were inserted into the control nanowire between island positions (seen in Fig. 2d), providing local potential wells to ensure that c-DW traverses only one island per pulse and provide a well-defined end position for the c-DW after each pulse.

The threshold current values were determined using simulation increments of 0.5×10^{12} A/m^2 and defined as follows; 'skip' mode: above minimum $\mathbf{J}$ to overcome magnetostatic attraction between c-DW and nanoisland and drive the c-DW across the nanoisland, and below maximum $\mathbf{J}$ satisfying $\mathbf{H}_{DW} + \mathbf{H}_{Oe} < \mathbf{H}_N$—and 'write' mode: above minimum $\mathbf{J}$ satisfying $\mathbf{H}_{DW} + \mathbf{H}_{Oe} \geq \mathbf{H}_N$ and below maximum $\mathbf{J}$ where induced nanoisland DWs leave a non-turbulent regime and begin exhibiting Walker breakdown, which can cause stochastic reversal failure by driving both i-DWs into the same nanoisland end. Functionality of both reversal modes in nanoisland arrays was investigated, with both modes acheiving switching as described above down to a minimum inter-island spacing of 60 nm, below which dipolar coupling between islands begins to interfere with the reversal process. The current densities employed here are on the high side, but similar to those employed in existing devices[46]. There is significant scope for reducing current density, with several relevant approaches investigated in the literature including material choice[47], nanowire geometry[48–50], or replacing the DW with another magnetic charge source such as a Skyrmion[51].

Existing solid-state magnetic reversal schemes require two control lines to address a single element in an array; typically two orthogonal sets of current lines above and below the array[35–38]. Here, the same control is achieved with a single set of lines, a reduction of n lines in an n-row array. The c-DW may be prepared electrically using previously described stripline-based schemes[44,52].

One-dimension RMC: reconfigurably gated waveguide. Magnonic device designs hinge on deterministic control of the magnon signal output, either via amplitude or phase modulation. Amplitude control has been demonstrated in two-state 'transistor'-like devices and via a 1D gateable RMC[11,13,21,23,53–56]. However, gate positions are static—hard-coded at the nanofabrication stage by distinct patterning of 'gate' nanoislands relative to the rest of array and microstate control is restricted to just two of the 2^N available states (in an N-island array) and reliant on global-field sequences. These designs function well and are important proofs of concept, but the reliance on global-field limits their utility in systems containing magnetically sensitive states and presents device integration challenges and static gate positions limit flexibility and scope. In addition, the number and location of distinctly patterned gate nanoislands affects the frequency and Q-factor of resonant modes even in the ungated state, causing functional behaviour to vary between arrays with different gate positions or numbers.

Here we present an RMC allowing reconfigurable current-controlled gating with no global-field requirement or differential nanoisland patterning. The design comprises a 1D nanoisland array situated above an underlying control nanowire. Selective nanoisland reversal is achieved by using current-pulses to shift the c-DW position relative to the array as described above. Our reversal scheme allows for a range of gate types, from single-island gating to more complex multi-island gates offering a range of functional benefits.

The RMC is depicted schematically in Fig. 3a, comprising 25 Py nanoislands of dimensions $350 \times 120 \times 5$ nm^3 with 60 nm inter-island spacing and 40×40 nm^2 cross-section Py control nanowire along the array long axis. The first four islands are covered by a 550 nm wide Au coplanar waveguide, using pulsed $\mathbf{H}_{Oe}$ to locally excite magnons via which propagate along the RMC via dipolar inter-island interactions. The nanoislands have stable Ising-like magnetization in the $\pm y$-direction, initialized here with $M = \hat{y}$ referred to as the 'ungated' state. Figure 3b–k illustrate magnon
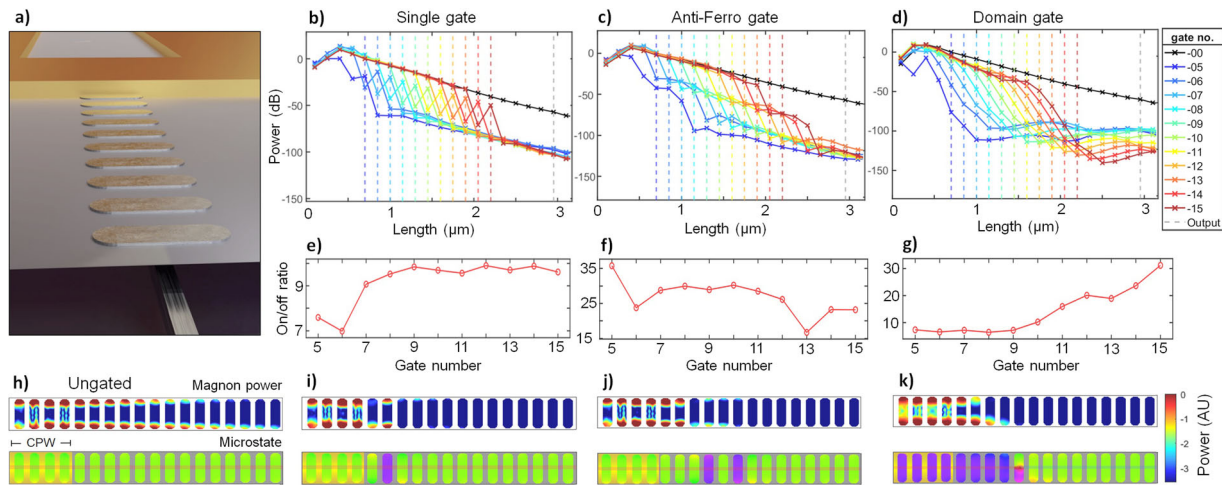
Fig. 3 Schematic of the one-dimensional reconfigurable magnonic crystal. Coplanar Au microwave waveguide is at image top and underlying domain wall-carrying control nanowire is shown protruding at image bottom. **b–d** Edge-mode spin-wave power vs. array position for **b** single, **c** 'antiferro' and **d** 'domain' gate types. Coplanar microwave waveguide covers islands 1–4. Nanoisland positions denoted by dashed vertical lines with power vs. position traces colour-coded by gate position. **e, f** Corresponding magnon 'on/off' ratio vs. gate position for each gate type, calculated from the ratio of integrated power at island 20 in the ungated to gated case. **h–k** Spatial power maps of resonant magnon edge mode for **h** ungated, **i** single, **j** 'antiferro' and **k** 'domain' gate types. Power is normalized to ungated case. Array microstate is shown with green (purple) representing unswitched (switched) islands magnetized in the positive y (negative-y) direction. Control nanowire is shown over array, coplanar Au waveguide covers islands 1–4. Control nanowire is in fully selective $h = 20$ nm reversal regime for all cases other than 'domain gate', which operates in low-power $h = 10$ nm regime.

power transmission through the RMC in a selection of array microstates. Figure 3h shows the spatial power map of the magnon edge mode centred on 2.1 GHz in the ungated array, with good magnon transmission throughout the array. Considering first the fully selective reversal mode (control nanowire at $h = 20$ nm above nanoislands), Fig. 3b, e, i show the 'single gate' case, where one nanoisland in the array is reversed to $M = -\hat{y}$ via a high-**J** 'write' c-DW traversal. Figure 3i shows magnon transmission strongly attenuated at the reversed gate island with 'on/off' ratios up to 10 observed (Fig. 3e), calculated from the ratio of integrated power at island 20 in the ungated to gated case.

One benefit of our reversal technique is the freedom to explore gating involving multiple reversed nanoislands. Figure 3c, f, j show one example of this, involving two reversed islands separated by an unreversed island. Termed an 'antiferromagnetic' (AFM)-type gate, on/off ratios are substantially improved to ~30 across a range of gate positions with a peak ratio of 35 at position 5. While the previous gate types may be accessed in the fully selective $h = 20$ nm reversal mode, the low-power reversal mode switches all nanoislands traversed by the c-DW so microstates containing isolated reversed islands in otherwise unreversed arrays are not possible. With this in mind, Fig. 3d, g, k show a $h = 10$ nm RMC in a gated state comprising continuously reversed nanoislands one on array side with the other side left unreversed, termed a 'domain'-type gate. The presence of the c-DW in the $h = 10$ mode introduces a 180° DW in the adjacent nanoisland from the influence of H_{DW}, seen in the Fig. 3k microstate. This is the stable relaxed state and serves to improve gating efficacy relative to domain-type gates prepared in the $h = 20$ nm mode which do not introduce 180° DWs to any nanoisland. The ratios acheived here compare well with existing designs, matching or outperforming the prior art[11,54–56] for a single-island gated 1D array RMC using differential patterning of the gate island. The domain-type gate perpared in the low-power, $h = 10$ nm reversal mode has the additional benefit of affecting the bulk-localized magnon mode more significantly than other gate cases, illustrated in Supplementary Fig. 1 with accompanying discussion in Supplementary Note 1.

Two-dimension RMC: reconfigurable filter. The 1D RMC above controls travelling $k \neq 0$ magnon modes. Here we present a second RMC design leveraging the reversal method to control standing-wave $k = 0$ magnons in a 2D nanoisland array. Manipulating frequency and intensity of standing-wave magnons allows for key functionality including opening and closing specific frequency channels and selective band-pass filtering, with enhanced q-factor and transmission/rejection ratios relative to travelling-wave magnons[27–34,57].

The RMC is depicted schematically in Fig. 4a, comprising adjacent columns of Py nanoislands each with a corresponding DW-carrying control nanowire. Columns are separated by a gap g_x and islands within a column by gap g_y. Adjacent columns are offset in the y-axis by a gap $\frac{g_y}{2}$ to optimize dipolar coupling and hence difference between spectra of distinct microstates. The array considered here has nanoisland dimensions $300 \times 94 \times 5$ nm^3 and inter-island spacings $g_x = 84$ nm, $g_y = 190$ nm. Dimensions and spacings were optimized for RMC gain functionality.

Figure 4b–d show three microstates termed 'ferromagnetic' (FM) (b), 'antiferromagnetic' (AFM) (c) and 'stripe' (d), accessible via shuttling c-DWs through control nanowires as described above. The RMC was prepared in each microstate and the spin-wave response studied after broadband excitation via an out-of-plane H_{Ext} sinc pulse. Figure 4e shows the resultant spin-wave spectra, with two distinct modes present for each microstate; a nanoisland-edge localized 1–3 GHz mode (f_{edge} of 2.43, 1.78 and 2.74 GHz for FM, AFM and stripe, respectively), and a nanoisland-centre localized 5–8 GHz mode, with spatial mode profiles displayed next to each peak. The cause of distinct modes in each microstate is the differing local field H_{loc} profile from nanoisland stray dipolar fields[58–65]. These are at their strongest at the nanoisland edges and it follows that the edge-localized modes display greater microstate sensitivity. This sensitivity allows for considerable mode control, with a frequency shift of $\Delta f = 0.96$ GHz achieved by transitioning between the AFM and stripe states, with the FM state providing an interstitial frequency midpoint.
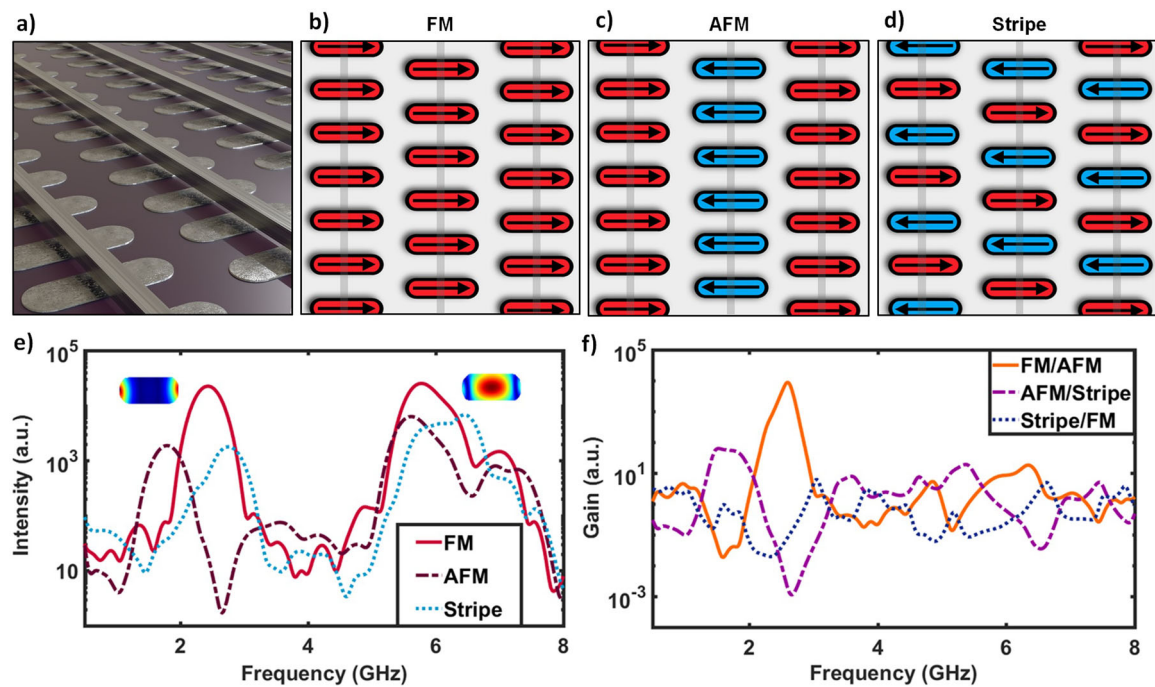
Fig. 4 Two-dimension magnonic crystal. a Schematic of the 2D magnonic crystal incorporating control nanowires above each column of the nanomagnet array. **b–d** Schematics of the **b** FM, **c** AFM and **d** 'stripe' microstates illustrating magnetization directions of each nanoisland and control-nanowire positions. **e** Spin-wave spectra of ferromagnetic (FM), antiferromagnetic (AFM) and 'stripe' microstates on a 4 × 6 nanoisland magnonic crystal. Each state shows two main resonances, an edge-localized mode (1–3 GHz) and a centrally localized mode (5–8 GHz). Spatial magnon power maps for each mode are displayed next to peaks. **f** Spin-wave amplitude gain achieved by transitioning between microstates, i.e., moving from FM to AFM state (solid orange line).

In addition to frequency shifting, microstate control affords substantial magnon amplitude modulation. Figure 4f shows the gain factor obtained by switching between the three microstates, with a gain of $\sim 9 \times 10^3$ achieved at the FM peak frequency $f = 2.43$ GHz by moving between the FM and AFM states, and a gain of $\sim 1 \times 10^3$ achieved at the AFM peak frequency $f = 2.74$ GHz by moving between the AFM and stripe states. The $h = 20$ nm fully selective mode is capable of accessing the entirety of the RMC's microstate space, the three states presented here are a representative selection of the potential functionality available. States such as 'AFM' where entire columns of nanoislands are reversed are accessible in the $h = 10$ nm low-power mode, with the added benefit that control nanowires need only be patterned for the reversed columns—a reduction of 50% in the AFM case. In addition, array geometries containing nanoislands at different angles such as square artificial spin ice[62,64] may be written by patterning control nanowires above and below the nanoislands at different angles. For instance, in the case of square artificial spin ice the y-axis control nanowires may be below the nanoislands and the x-axis control wires above.

The states in Fig. 4 are chosen as they have identical $\mathbf{H}_{loc}$ values at each nanoisland (relative to the nanoisland magnetization) so magnon modes are clearly defined. However, the writing technique enables access to all microstates, including states with different $\mathbf{H}_{loc}$ values at different array positions and hence multiple magnon modes. These mixed-$\mathbf{H}_{loc}$ microstates may be finely tailored, providing control over mode amplitude, frequency, bandwidth and the number of active modes. Detailed discussion of mixed states and their spectra is presented in Supplementary Fig. 2 and Supplementary Note 2 including the effects of gradual transitions between the FM, AFM and stripe states. Both RMC described here are suitable for signal readout via optical (micro-focused Brillouin light spectroscopy) or electrical (FM resonance) means.

Conclusions. In this work, we outline a powerful fully solid-state magnetic writing technique, allowing total microstate control without global fields and excellent integration propspects for on-chip systems. The technique allows a class of nanomagnetic systems deriving versatile functionality from a broad range of microstates to become viable candidates for technological advancement, as evidenced by the two RMC designs presented here.

By opening the entire range of microstates for exploration and exploitation, the writing technique described here invites a host of novel nanomagnetic system designs, in addition to the refinement and enhancement of existing designs which are currently limited to narrow regions of microstate space. Functional benefits are offered across diverse applications including neuromorphic logic and superconducting vortex control.

Although Py is employed as the FM material throughout this work, it is chosen for its ubiquity and familiarity in current nanomagnetic systems and near-zero shape anisotropy rather than ideal magnonic performance. Low-damping ferromagnets such as YIG[66], various Heusler alloys[67,68] and more simple bimetallic alloys such as CoFe[69] have superior characteristics for low-loss, longer distance magnon transmission, enhancing functionality of the proposed and related devices incorporating our reversal method. In addition, the array dimensions reported here represent a proof-of-concept and are chosen to be readily fabricated using widely available equipment and techniques. Reducing array separation and fine tuning dimensions will enhance the spectral effects reported here and the related functionalities. We have focused here on magnetic reversal of Ising-like nanoelements. Prior studies have demonstrated injection of 360° DWs[41] and Skyrmions using related locally divergent stray fields (magnetic force microscope tips in these cases) in nanostructures and writing states in nanodisks[70]. The DW-based writing method is highly suitable for integration with such writing schemes, offering substantial future scope.
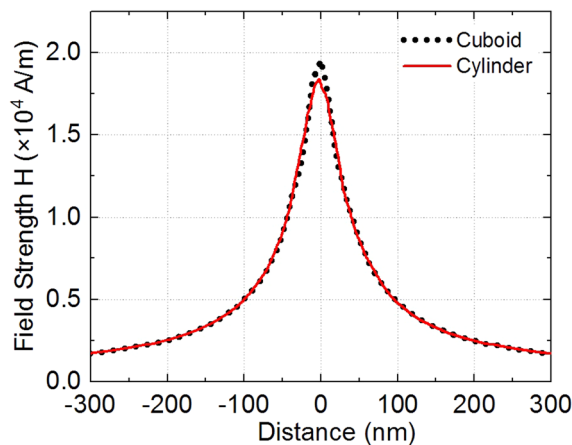
Fig. 5 Field profiles of current-carrying cylindrical and cuboid nanowires.
Field profile experienced by a nanoisland that is positioned $h = 10$ nm below
an infinitely long cylinder and cuboid. There is a small discrepancy of 0.15×10^4 Am^{-1} around $x = 0$, which can be minimized by adjusting the value of the
current density.

Methods

Reversal method. All simulations were performed using MuMax3 [71–73]. Magnetic
parameters for Py (Ni$_{80}$Fe$_{20}$) of $A = 13$ pJ/m, $\alpha = 0.02$ and $M_s = 800 \times 10^3$ kA/m. A
cell size of $4 \times 4 \times 4$ nm^3 is used and two numerical solvers are employed at different
stages of the simulation: (i) an equilibrium head-to-head transverse domain wall is
formed in the nanowire by minimizing the total energy of the system using the
conjugate gradient method and (ii) the temporal evolution of the system is computed
by solving the modified version of Landau–Lifshitz–Gilbert equation that includes
terms for spin-transfer-torque using the Dormand–Prince method (RK45) [72]. The
advantage of the Dormand–Prince method is adaptive time steps, dependent on the
error magnitude at each iteration, reducing computational intensity.

Boundary conditions are applied to the current-carrying nanowire ends to
remove surface charges and associated stray fields, simulating a quasi-infinite wire.
A 5 nm window of spins at wire ends are fixed to eliminate turbulent fluctuations
when an electric current is applied. $\mathbf{H}_{Oe}$ in and around the current-carrying
nanowire is simulated by solving Maxwell's equation $\nabla \times \mathbf{B} = \mu_0 \mathbf{J}$, approximating
the wire as an infinitely long cylinder and adding the corresponding vector field
component to each of the finite-difference cells. The validity of the cylindrical-wire
assumption was examined using Finite Element Method Magnetics [74], with the
comparison between $\mathbf{H}_{Oe}$ profiles of cylindrical and cuboid nanowires shown in
Fig. 5. Near-identical field profiles are seen, with the small discrepancy for low
distances from the nanowire accounted for in the reversal simulations by varying $\mathbf{J}$
to match the cuboid case.

Reconfigurably gated magnonic waveguide. To remove stochasticity from
nanoisland edge-curl states (i.e., s- and c-states) and allow direct comparison between
gating types and positions, arrays are relaxed in a 1 mT global field, applied 5° above
in the positive x-direction.

Magnons are excited with a 20 mT sinc pulse in the z-direction applied locally
under the Au waveguide, exciting modes up to 20 GHz. The function has a
sinusoidal wavelength of 550 nm along the array long axis, covering the first four
nanoislands under the waveguide (see Fig. 3h) for visual of waveguide position).
The pulse begins at 50 ps and the magnetization is recorded every 25 ps for 800
time steps, a total simulation time of 40 ns.

For both RMC simulations, the damping parameter α was reduced to 0.006 for
greater correspondence with experiment. Simulation cell sizes of 5 nm were used in
all dimensions.

Reconfigurable magnonic filter. A quasi-infinite array is simulated using periodic
boundary conditions, with a two-column, seven island per-column unit cell. Spin-
waves are excited by an out-of-plane $\mathbf{H}_{Ext}$ sinc pulse applied uniformly across the
array, exciting modes between 0.1 and 25 GHz. Simulation cell sizes of 3 nm × 2.2
nm × 5 nm were used in the x, y and z directions respectively.

Magnons are excited with a 20 mT sinc pulse in the z-direction, exciting modes
up to 25 GHz. The function is applied across the entire system. The pulse begins at
50 ps and the magnetization is recorded every 20 ps for 256 time steps, a total
simulation time of 5.12 ns.

Data availability

The datasets generated during and/or analysed during the current study are available
from the corresponding author on reasonable request.

References

1. Romera, M. et al. Vowel recognition with four coupled spin-torque nano-
oscillators. *Nature* **563**, 230–234 (2018).
2. Mizrahi, A. et al. Neural-like computing with populations of superparamagnetic
basis functions. *Nat. Commun.* **9**, 1–11 (2018).
3. Grollier, J. et al. Neuromorphic spintronics. *Nat. Electron.* **3**, 360–370 (2020).
4. Sangwan, V. K. & Hersam, M. C. Neuromorphic nanoelectronic materials. *Nat.
Nanotechnol.* **15**, 517–528 (2020).
5. Brächer, T. & Pirro, P. An analog magnon adder for all-magnonic neurons. *J.
Appl. Phys.* **124**, 152119 (2018).
6. Wang, Y.-L. et al. Switchable geometric frustration in an artificial-spin-
ice–superconductor heterosystem. *Nat. Nanotechnol.* **13**, 560–565 (2018).
7. Sadovskyy, I. A., Wang, Y., Xiao, Z.-L., Kwok, W.-K. & Glatz, A. Effect of
hexagonal patterned arrays and defect geometry on the critical current of
superconducting films. *Phys. Rev. B* **95**, 075303 (2017).
8. Rollano, V. et al. Topologically protected superconducting ratchet effect
generated by spin-ice nanomagnets. *Nanotechnology* **30**, 244003 (2019).
9. Dobrovolskiy, O. et al. Magnon–fluxon interaction in a ferromagnet/
superconductor heterostructure. *Nat. Phys.* **15**, 477–482 (2019).
10. Grundler, D. Reconfigurable magnonics heats up. *Nat. Phys.* **11**, 438 (2015).
11. Haldar, A., Kumar, D. & Adeyeye, A. O. A reconfigurable waveguide for energy-
efficient transmission and local manipulation of information in a nanomagnetic
device. *Nat. Nanotechnol.* **11**, 437 (2016).
12. Krawczyk, M. & Grundler, D. Review and prospects of magnonic crystals and
devices with reprogrammable band structure. *J. Phys. Condens. Matter* **26**,
123202 (2014).
13. Wang, Q. et al. Voltage-controlled nanoscale reconfigurable magnonic crystal.
Phys. Rev. B **95**, 134433 (2017).
14. Topp, J., Heitmann, D., Kostylev, M. P. & Grundler, D. Making a
reconfigurable artificial crystal by ordering bistable magnetic nanowires. *Phys.
Rev. Lett.* **104**, 207205 (2010).
15. Neusser, S. & Grundler, D. Magnonics: spin waves on the nanoscale. *Adv.
Mater.* **21**, 2927–2932 (2009).
16. Kruglyak, V., Demokritov, S. & Grundler, D. Magnonics. *J. Phys. D Appl. Phys.*
43, 264001 (2010).
17. Khitun, A., Bao, M. & Wang, K. L. Magnonic logic circuits. *J. Phys. D Appl.
Phys.* **43**, 264005 (2010).
18. Khitun, A. & Wang, K. L. Non-volatile magnonic logic circuits engineering. *J.
Appl. Phys.* **110**, 034306 (2011).
19. Lenk, B., Ulrichs, H., Garbs, F. & Münzenberg, M. The building blocks of
magnonics. *Phys. Rep.* **507**, 107–136 (2011).
20. Chumak, A. V., Vasyuchka, V. I., Serga, A. A. & Hillebrands, B. Magnon
spintronics. *Nat. Phys.* **11**, 453–461 (2015).
21. Chumak, A., Serga, A. & Hillebrands, B. Magnonic crystals for data
processing. *J. Phys. D Appl. Phys.* **50**, 244001 (2017).
22. Wang, Q. et al. Integrated magnonic half-adder. Preprint at https://doi.org/
10.1038/s41928-020-00485-6 (2019).
23. Fischer, T. et al. Experimental prototype of a spin-wave majority gate. *Appl.
Phys. Lett.* **110**, 152401 (2017).
24. Wintz, S. et al. Magnetic vortex cores as tunable spin-wave emitters. *Nat.
Nanotechnol.* **11**, 948–953 (2016).
25. Sluka, V. et al. Emission and propagation of 1d and 2d spin waves with
nanoscale wavelengths in anisotropic spin textures. *Nat. Nanotechnol.* **14**,
328–333 (2019).
26. Liu, C. et al. Current-controlled propagation of spin waves in antiparallel,
coupled domains. *Nat. Nanotechnol.* **14**, 691–697 (2019).
27. Sadovnikov, A., Gubanov, V., Sheshukova, S., Sharaevskii, Y. P. & Nikitov, S.
Spin-wave drop filter based on asymmetric side-coupled magnonic crystals. *Phys.
Rev. Appl.* **9**, 051002 (2018).
28. Wang, Q., Zeng, L., Lei, M. & Bi, K. Tunable metamaterial bandstop filter based
on ferromagnetic resonance. *AIP Adv.* **5**, 077145 (2015).
29. Semenova, E. & Berkov, D. Spin wave propagation through an antidot
lattice and a concept of a tunable magnonic filter. *J. Appl. Phys.* **114**, 013905
(2013).
30. Ma, F. et al. Micromagnetic study of spin wave propagation in bicomponent
magnonic crystal waveguides. *Appl. Phys. Lett.* **98**, 153107 (2011).
31. Kim, S.-K., Lee, K.-S. & Han, D.-S. A gigahertz-range spin-wave filter composed
of width-modulated nanostrip magnonic-crystal waveguides. *Appl. Phys. Lett.* **95**,
082507 (2009).
32. Mamica, S. & Krawczyk, M. Reversible tuning of omnidirectional band gaps in
two-dimensional magnonic crystals by magnetic field and in-plane squeezing.
Phys. Rev. B **100**, 214410 (2019).

33. Mamica, S., Krawczyk, M. & Grundler, D. Nonuniform spin-wave softening in two-dimensional magnonic crystals as a tool for opening omnidirectional magnonic band gaps. *Phys. Rev. Appl.* **11**, 054011 (2019).

34. Graczyk, P. et al. Magnonic band gap and mode hybridization in continuous permalloy films induced by vertical dynamic coupling with an array of permalloy ellipses. *Phys. Rev. B* **98**, 174420 (2018).

35. Kawahara, T. et al. 2mb spin-transfer torque ram (spram) with bit-by-bit bidirectional current write and parallelizing-direction current read. Digest of Technical Papers. In *2007 IEEE Int. Solid-State Circuits Conference* 480–617 (IEEE, 2007).

36. Zhao, W., Belhaire, E., Chappert, C. & Mazoyer, P. Spin transfer torque (stt)-mram–based runtime reconfiguration fpga circuit. *ACM Trans. Embedded Comput. Syst.* **9**, 1–16 (2009).

37. Kawahara, T. et al. 2 mb spram (spin-transfer torque ram) with bit-by-bit bidirectional current write and parallelizing-direction current read. *IEEE J. Solid State Circuits* **43**, 109–120 (2008).

38. Kawahara, T., Ito, K., Takemura, R. & Ohno, H. Spin-transfer torque ram technology: review and prospect. *Microelectron. Reliab.* **52**, 613–627 (2012).

39. Gartside, J. C. et al. Realization of ground state in artificial kagome spin ice via topological defect-driven magnetic writing. *Nat. Nanotechnol.* **13**, 53 (2018).

40. Wang, Y.-L. et al. Rewritable artificial magnetic charge ice. *Science* **352**, 962–966 (2016).

41. Gartside, J., Burn, D., Cohen, L. & Branford, W. A novel method for the injection and manipulation of magnetic charge states in nanostructures. *Sci. Rep.* **6**, 32864 (2016).

42. Mermin, N. D. The topological theory of defects in ordered media. *Rev. Mod. Phys.* **51**, 591 (1979).

43. Tchernyshyov, O. & Chern, G.-W. Fractional vortices and composite domain walls in flat nanomagnets. *Phys. Rev. Lett.* **95**, 197204 (2005).

44. Pushp, A. et al. Domain wall trajectory determined by its fractional topological edge defects. *Nat. Phys.* **9**, 505–511 (2013).

45. Wang, X., Yan, P., Shen, Y., Bauer, G. & Wang, X. Domain wall propagation through spin wave emission. *Phys. Rev. Lett.* **109**, 167209 (2012).

46. Xu, Y., Awschalom, D. & Nitta, J. *Handbook of Spintronics* (Springer, The Netherlands, 2016).

47. Li, S., Nakamura, H., Kanazawa, T., Liu, X. & Morisako, A. Domain wall motion induced by low current density in tbfeco wire with perpendicular magnetic anisotropy. *J. Magn. Soc. Jpn.* **34**, 333–336 (2010).

48. Yamaguchi, A., Yano, K., Tanigawa, H., Kasai, S. & Ono, T. Reduction of threshold current density for current-driven domain wall motion using shape control. *Jpn J. Appl. Phys.* **45**, 3850 (2006).

49. Tretiakov, O. A., Liu, Y. & Abanov, A. Minimization of ohmic losses for domain wall motion in a ferromagnetic nanowire. *Phys. Rev. Lett.* **105**, 217203 (2010).

50. Fangohr, H., Chernyshenko, D. S., Franchin, M., Fischbacher, T. & Meier, G. Joule heating in nanowires. *Phys. Rev. B* **84**, 054437 (2011).

51. Kang, W. et al. Voltage controlled magnetic skyrmion motion for racetrack memory. *Sci. Rep.* **6**, 23164 (2016).

52. Burn, D., Chadha, M. & Branford, W. Dynamic dependence to domain wall propagation through artificial spin ice. *Phys. Rev. B* **95**, 104417 (2017).

53. Chumak, A. V., Serga, A. A. & Hillebrands, B. Magnon transistor for all-magnon data processing. *Nat. Commun.* **5**, 1–8 (2014).

54. Cornelissen, L., Liu, J., Van Wees, B. & Duine, R. Spin-current-controlled modulation of the magnon spin conductance in a three-terminal magnon transistor. *Phys. Rev. Lett.* **120**, 097702 (2018).

55. Wu, H. et al. Magnon valve effect between two magnetic insulators. *Phys. Rev. Lett.* **120**, 097205 (2018).

56. Cramer, J. et al. Magnon detection using a ferroic collinear multilayer spin valve. *Nat. Commun.* **9**, 1–7 (2018).

57. Tacchi, S. et al. Universal dependence of the spin wave band structure on the geometrical characteristics of two-dimensional magnonic crystals. *Sci. Rep.* **5**, 10367 (2015).

58. Gliga, S., Kákay, A., Hertel, R. & Heinonen, O. G. Spectral analysis of topological defects in an artificial spin-ice lattice. *Phys. Rev. Lett.* **110**, 117205 (2013).

59. Zhou, X., Chua, G.-L., Singh, N. & Adeyeye, A. O. Large area artificial spin ice and anti-spin ice ni80fe20 structures: static and dynamic behavior. *Adv. Funct. Mater.* **26**, 1437–1444 (2016).

60. Dion, T. et al. Tunable magnetization dynamics in artificial spin ice via shape anisotropy modification. *Phys. Rev. B* **100**, 054433 (2019).

61. Arroo, D. M., Gartside, J. C. & Branford, W. R. Sculpting the spin-wave response of artificial spin ice via microstate selection. *Phys. Rev. B* **100**, 214425 (2019).

62. Iacocca, E., Gliga, S., Stamps, R. L. & Heinonen, O. Reconfigurable wave band structure of an artificial square ice. *Phys. Rev. B* **93**, 134420 (2016).

63. Jungfleisch, M. B. et al. High-frequency dynamics modulated by collective magnetization reversal in artificial spin ice. *Phys. Rev. Appl.* **8**, 064026 (2017).

64. Jungfleisch, M. et al. Dynamic response of an artificial square spin ice. *Phys. Rev. B* **93**, 100401 (2016).

65. Bhat, V., Heimbach, F., Stasinopoulos, I. & Grundler, D. Magnetization dynamics of topological defects and the spin solid in a kagome artificial spin ice. *Phys. Rev. B* **93**, 140401 (2016).

66. Chang, H. et al. Nanometer-thick yttrium iron garnet films with extremely low damping. *IEEE Magn. Lett.* **5**, 1–4 (2014).

67. Sebastian, T. et al. Low-damping spin-wave propagation in a micro-structured co2mn0. 6fe0. 4si heusler waveguide. *Appl. Phys. Lett.* **100**, 112402 (2012).

68. Nayak, A. K. et al. Magnetic antiskyrmions above room temperature in tetragonal heusler materials. *Nature* **548**, 561–566 (2017).

69. Schoen, M. A. et al. Ultra-low magnetic damping of a metallic ferromagnet. *Nat. Phys.* **12**, 839–842 (2016).

70. Stenning, K. et al. Magnonic bending, phase shifting and interferometry in a 2d reconfigurable nanodisk crystal. Preprint at arXiv:2008.06451 (2020).

71. Vansteenkiste, A. & Van de Wiele, B. Mumax: a new high-performance micromagnetic simulation tool. *J. Magn. Magn. Mater.* **323**, 2585–2591 (2011).

72. Vansteenkiste, A. et al. The design and verification of mumax3. *AIP Adv.* **4**, 107133 (2014).

73. Leliaert, J. et al. Fast micromagnetic simulations on gpu-recent advances made with. *J. Phys. D Appl. Phys.* **51**, 123002 (2018).

74. Meeker, D. Finite element method magnetics. *FEMM* **4**, 32 (2010).

75. Imperial college research computing service. Available at: https://doi.org/10.14469/hpc/2232. https://www.imperial.ac.uk/admin-services/ict/self-service/research-support/rcs/impact/citing-the-service/.

Acknowledgements

Author contributions

J.C.G., D.M.A. and W.R.B. conceived the work. D.M.A. wrote initial code for simulation of the reversal method and generation of magnon spectra. S.G.J. and S.Y.Y. performed simulations of the reversal method, including the basic functional concept, the two distinct modes and simulations including current-driving DWs using spin-transfer torque. S.G.J. and S.Y.Y. further developed and expanded the simulation code with contributions from D. M.A. J.C.G., A.V., T.D. and K.D.S. performed simulations of the RMC systems, with J.C.G., A.V. and K.S. working primarily on the 2D RMC and TD working primarily on the 1D RMC. CGI visualizations were designed and rendered by K.D.S. J.C.G. drafted the manuscript, with contributions from S.G.J. and S.Y.Y. in the 'reversal method' subsection of the 'simulation details' section.

Competing interests

The authors declare no competing interests.

Additional information

Supplementary information is available for this paper at https://doi.org/10.1038/s42005-020-00487-y.

Correspondence and requests for materials should be addressed to J.C.G.

Reprints and permission information is available at http://www.nature.com/reprints

Publisher's note Springer Nature remains neutral with regard to jurisdictional claims in published maps and institutional affiliations.